Available online at www.sciencedirect.com
ScienceDirect
Trans. Nonferrous Met. Soc. China 32(2022) 3136−3148
Transactions of Nonferrous Metals Society of China
www.tnmsc.cn

Cobalt recovery and microspherical cobalt tetroxide preparation from ammonia leaching solution of spent lithium-ion batteries

Jian-cheng YU[1,2], Bao-zhong MA[1,2], Shuang SHAO[1,2],
Cheng-yan WANG[1,2], Yong-qiang CHEN[1,2], Wen-juan ZHANG[1,2]

1. State Key Laboratory of Advanced Metallurgy,
University of Science and Technology Beijing, Beijing 100083, China;
2. School of Metallurgical and Ecological Engineering,
University of Science and Technology Beijing, Beijing 100083, China

Received 12 July 2021; accepted 7 December 2021

Abstract: A process for recovering Co and preparing microspherical Co_3O_4 through NH_3 distillation and phase transformation from ammoniacal solution was investigated. As the basis of thermodynamics, the solubility of Co at different NH_3 and CO_3^{2-} concentrations was studied, and then the effects of different NH_3 distillation conditions on Co recovery rate were discussed. Over 94% Co and 96% NH_3 were recovered through NH_3 distillation, and the cobalt was precipitated in form of cobalt carbonate ammonium compound salt. Through the analysis of the formation mechanism of the precursor, the precipitation process of cobalt could be divided into two stages, and the cobalt precipitation rate was significantly accelerated in the second stage. In phase transformation, the effect of temperature on the roasted product was investigated. The microspherical Co_3O_4 with a microporous structure was prepared at 300 °C, and Co_3O_4 with a mesoporous structure and high-spin state was obtained at 750 °C.

Key words: spent lithium-ion batteries; NH_3 distillation; Co recovery; mechanism analysis; Co_3O_4 preparation

1 Introduction

In recent years, with the rapid development of the new energy automobile industry, the demand for lithium-ion batteries (LIBs) has exploded. It is estimated that the battery demand for electric vehicles will be 0.78−2.2 TW·h/a in 2030 [1], which will generate a large number of spent LIBs inevitably. Hence, comprehensive utilization of spent LIBs can not only reduce their harm to the environment but also recover valuable metals, such as Li, Ni, and Co [2−4]. The traditional hydrometallurgical recycling process is widely used in industrial production due to low energy consumption and high metal recovery rate. However, there are still some shortcomings in the actual application, for example, the pre-sorting technology is immature, and the expensive reducing agent is needed during the leaching process [5,6]. Therefore, it is very necessary to develop a cleaner and more efficient process. Based on the previous research [7,8], a breakthrough method of comprehensive recycling $LiNi_xCo_yMn_zO_2$ LIBs was proposed by our research team.

Firstly, the spent LIBs do not need to be pre-sorted, which avoids the loss of valuable metals during the sorting process. After simple discharge and crushing, the spent LIBs are roasted directly with the reducing agent. Then, Li can be extracted

Corresponding author: Bao-zhong MA, Tel: +86-18601365281, E-mail: bzhma_ustb@yeah.net;
Cheng-yan WANG, Tel: +86-13651380586, E-mail: chywang@yeah.net
DOI: 10.1016/S1003-6326(22)66009-6

preferentially through carbonated water leaching. Ni, Co, and Cu exist in the leaching residue. Compared with the traditional ammonia or acid leaching process, the loss of Li is lower and the obtained Li_2CO_3 products are purer [9−11]. Secondly, Ni, Co, and Cu are selectively leached into the solution by NH_3−$(NH_4)_2CO_3$ leaching, while Al, Mn, and Fe are not leached, which simplifies the purification process. In the NH_3 leaching solution, Ni and Cu can be recovered in the form of sulfate after solvent extraction [12,13]. However, Co exists in form of $Co(NH_3)_6^{3+}$, which has a higher complexing constant ($K[Co(NH_3)_6^{3+}]=10^{35.2}$) and is not easily recovered [14−16]. As the last part of the whole process, the recovery of Co from the NH_3 leaching solution can not only avoid the waste of resources but also has important significance for the circulation of ammonia and water.

At present, the method for recovering Co from the ammoniacal system is to add Na_2S or $(NH_4)_2S$ to form the CoS precipitate, CoS is dissolved by acid and then the $CoSO_4$ product is obtained by solvent extraction [13]. In addition, Co can also be recovered by adding a reducing agent and alkali to obtain $Co(OH)_2$ [17]. Unfortunately, these methods produce a large amount of wastewater containing acid or alkali, which is not conducive to the sustainability of the whole process.

Therefore, the focus of this work is to recover Co from the NH_3 leaching solution efficiently and economically. The NH_3 distillation and phase transformation were proposed to recover Co from the ammoniacal solution. Firstly, the NH_3 distillation process was studied systematically, especially the effects of initial Co concentration, evaporation volume, and evaporation velocity on Co recovery rate. Then, the influences of phase transformation temperature on the properties of the product were discussed. During the entire process, Co can be recovered efficiently. NH_3 and residual liquid can be returned to the leaching stage and no wastewater is produced. This research suggested a promising and reliable method for Co recovery from the ammoniacal solution. It can also provide a reference for NH_3 leaching of other Co-containing resources, such as the reduction roasting–NH_3 leaching of laterite nickel ore, and NH_3 leaching of zinc plant purification residue, etc.

2 Experimental

2.1 Reagents and procedures

Reagents include $CoCO_3$, $NH_3·H_2O$ solution, and $(NH_4)_2CO_3$, which were obtained from Sinopharm Chemical Reagent Co., Ltd. All the reagents used in the experiments were of analytical grade. For each test, an appropriate amount of the solution was placed into a three-necked flask for heating. The stirring speed was 600 r/min, and the evaporation velocity was controlled by the changes in temperature. When the evaporation volume is fixed, at different temperatures, the time to reach the end of NH_3 distillation is different. Given that the evaporation velocity is a more common indicator in industry, hence, Eq. (1) was used to calculate the evaporation velocity (v_{ev}):

$$v_{ev}=\frac{V_0-V_f}{t} \tag{1}$$

where V_0 is the initial solution volume, mL; V_f is the residual solution volume, mL; t is the evaporation time, h.

After the NH_3 distillation process was completed, the precursor was roasted in a muffle furnace, and Co concentration in the residual liquor was measured.

2.2 Analysis methods

Co concentration in the solution before and after NH_3 distillation was analyzed with an ICP-OES system (Optima 7000DV, PerkinElmer) after dilution with deionized water, and NH_3−N was analyzed with a multiparameter water quality detector (5B−3B [V8], Lianhua Tech). The surface morphology and elemental distribution of the precursor were analyzed with a scanning electron microscopy (SEM) system (JSM−7001F) and energy dispersive X-ray spectroscopy (EDS) system (BRUKER XFlash5010), respectively. X-ray photoelectron spectroscopy (XPS) system (AXIS Ultra) and an iN10MX FTIR spectrometer were used in characterizing the valence states of elements and functional groups of the precursor. Mass loss and heat change in the precursor were analyzed using a thermogravimetric analyzer (STA409C) under an air atmosphere at a heating rate of 10 °C/min. The composition and morphology of the roasted product were analyzed through SEM and

X-ray diffraction (XRD) with a Rigaku Ultima IV diffractometer (Cu K_α). The textural characteristics of the roasted products were obtained from N_2 adsorption−desorption isotherms, and isotherms were measured using an ASAP 2020 micrometric instrument at −196 °C. The specific surface areas of the roasted products were estimated with the Brunauer−Emmett−Teller (BET) method, and pore size distributions were estimated using the Barrett–Joyner–Halenda method.

3 Results and discussion

3.1 Thermodynamic fundamentals

In the ammonia−ammonium carbonate (AAC) system, the concentration of each ion is related to pH value. When total carbon concentration (c_C) and total ammonia concentration (c_N) are assumed to be constant, the relationship between total cobalt concentration (c_{Co}) and pH can be obtained according to the equilibrium of chemical reactions shown in Table 1 and mass balance equations of phase transformation (Table 2) [18,19]. The results are shown in Fig. 1. The conditions of Fig. 1(a) are fixed, c_C=1.5 mol/L, and c_N values vary. c_{Co} increases with the increase of c_N because of the stability of $Co(NH_3)_i^{2+}$ (i=1−6), which gradually increases when i increases from 1 to 6 [20]. The conditions of Fig. 1(b) are fixed, c_N=6 mol/L, and c_C values vary. As shown in Fig. 1(b), because $Co(NH_3)_i^{2+}$ (i=1−3), which has a lower complexing constant, reacts with CO_3^{2-} to form $CoCO_3$, c_{Co} decreases with increasing c_C [21].

From the perspective of the influence of pH value on the Co concentration, as shown in Fig. 1, when the pH value increases to 10.0, c_{Co} reaches a

Table 1 Equilibrium reactions and constants for AAC system at 298 K

No.	Equilibrium reaction	Equilibrium constant equation	lg K
1	$Co^{2+}+NH_3=Co(NH_3)^{2+}$	$K_1=[Co(NH_3)^{2+}]/[Co^{2+}][NH_3]$	2.11
2	$Co^{2+}+2NH_3=Co(NH_3)_2^{2+}$	$K_2=[Co(NH_3)_2^{2+}]/[Co^{2+}][NH_3]^2$	3.74
3	$Co^{2+}+3NH_3=Co(NH_3)_3^{2+}$	$K_3=[Co(NH_3)_3^{2+}]/[Co^{2+}][NH_3]^3$	4.79
4	$Co^{2+}+4NH_3=Co(NH_3)_4^{2+}$	$K_4=[Co(NH_3)_4^{2+}]/[Co^{2+}][NH_3]^4$	5.55
5	$Co^{2+}+5NH_3=Co(NH_3)_5^{2+}$	$K_5=[Co(NH_3)_5^{2+}]/[Co^{2+}][NH_3]^5$	5.73
6	$Co^{2+}+6NH_3=Co(NH_3)_6^{2+}$	$K_6=[Co(NH_3)_6^{2+}]/[Co^{2+}][NH_3]^6$	5.11
7	$Co^{2+}+CO_3^{2-}=CoCO_3(s)$	$K_7=1/[Co^{2+}][CO_3^{2-}]$	12.8
8	$Co^{2+}+2OH^-=Co(OH)_2(s)$	$K_8=1/[Co^{2+}][OH^-]^2$	14.9
9	$Co^{2+}+H_2O=CoOH^++H^+$	$K_9=[CoOH^+][H^+]/[Co^{2+}]$	–9.75
10	$Co^{2+}+2OH^-=Co(OH)_2$	$K_{10}=[Co(OH)_2]/[Co^{2+}][OH^-]^2$	9.20
11	$Co^{2+}+3OH^-=Co(OH)_3^-$	$K_{11}=[Co(OH)_3^-]/[Co^{2+}][OH^-]^3$	10.50
12	$Co(OH)_2(s)+2OH^-=Co(OH)_4^{2-}$	$K_{12}=[Co(OH)_4^{2-}]/[OH^-]^2$	–5.10
13	$H_2O=H^++OH^-$	$K_{13}=[H^+][OH^-]$	–14.0
14	$HCO_3^-=H^++CO_3^{2-}$	$K_{14}=[H^+][CO_3^{2-}]/[HCO_3^-]$	–10.4
15	$H_2CO_3=H^++HCO_3^-$	$K_{15}=[H^+][HCO_3^-]$	–6.35
16	$NH_3+H^+=NH_4^+$	$K_{16}=[NH_4^+]/[H^+][NH_3]$	9.27

Table 2 Mass balance equations of phase transformation for AAC system at 298 K

Parameter	Mass balance equations of phase transformation
c_C	$c_C=[CO_3^{2-}]+[HCO_3^-]+[H_2CO_3]$
c_N	$c_N=[NH_3]+[NH_4^+]+[Co(NH_3)^{2+}]+2[Co(NH_3)_2^{2+}]+3[Co(NH_3)_3^{2+}]+4[Co(NH_3)_4^{2+}]+5[Co(NH_3)_5^{2+}]+6[Co(NH_3)_6^{2+}]$
c_{Co}	$c_{Co}=[Co^{2+}]+[Co(NH_3)^{2+}]+[Co(NH_3)_2^{2+}]+[Co(NH_3)_3^{2+}]+[Co(NH_3)_4^{2+}]+[Co(NH_3)_5^{2+}]+[Co(NH_3)_6^{2+}]$, $[Co^{2+}]=\min\{10^{-12.8}/[CO_3^{2-}], 10^{13.1-2pH}\}$

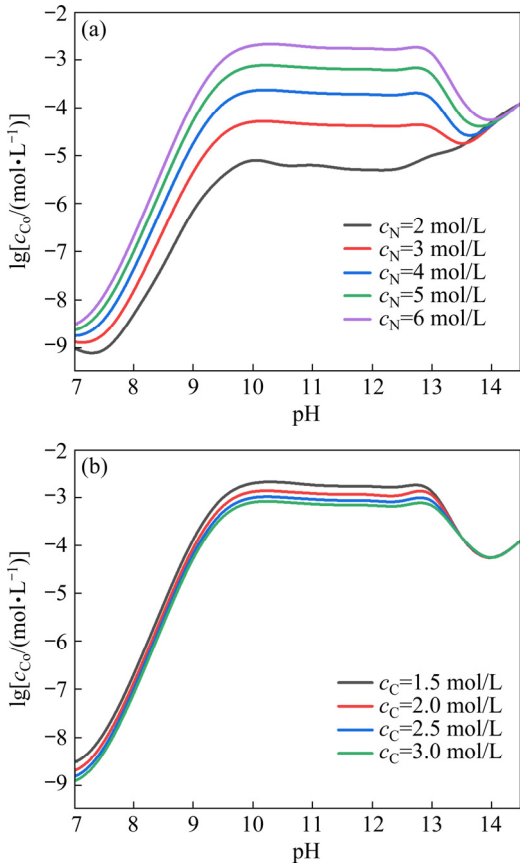

Fig. 1 lg c_{Co}–pH of AAC system at 298 K: (a) c_C= 1.5 mol/L; (b) c_N=6 mol/L

maximum value. This is also the optimal pH value for NH_3 leaching, which is consistent with many studies on controlling pH≈10 during the NH_3 leaching process of spent LIBs [22,23]. Although the theoretical solubility of Co remains high when the pH value increases, a high pH value causes the NH_3 concentration to increase significantly. When 13<pH<14, the structure of cobalt–ammonia complex ($Co(NH_3)_n^{2+}$) is destroyed, and $Co(OH)_2$ precipitates out of the solution. Therefore, the Co concentration starts to decrease at pH=13. However, under strong alkaline conditions (pH>14), Co mainly exists in the form of hydroxyl complex ions ($Co(OH)_i^{2-i}$), and the Co concentration increases with the increase of pH value in this range [19].

According to the above analysis, the decrease in c_C and increase in c_N are beneficial to the dissolution of Co in AAC solutions, which provides a thermodynamic basis for the NH_3 distillation process. The increase of the solution temperature makes a large amount of NH_3 volatilize, which will facilitate the decomposition of the $Co(NH_3)_6^{3+}$. Besides, the volatilization of ammonia also reduces the pH of the solution, and the decrease in the solution volume increases the probability of the combination of CO_3^{2-} and Co ions, which will also facilitate the precipitation of Co.

3.2 Effect of parameters on Co recovery

When the temperature of the solution reaches 94 °C, the solution starts to boil, the balance of cobalt–ammonia complex is broken, NH_3 starts to volatilize, and Co precipitates from the solution gradually. Figure 2(a) shows the effect of initial Co

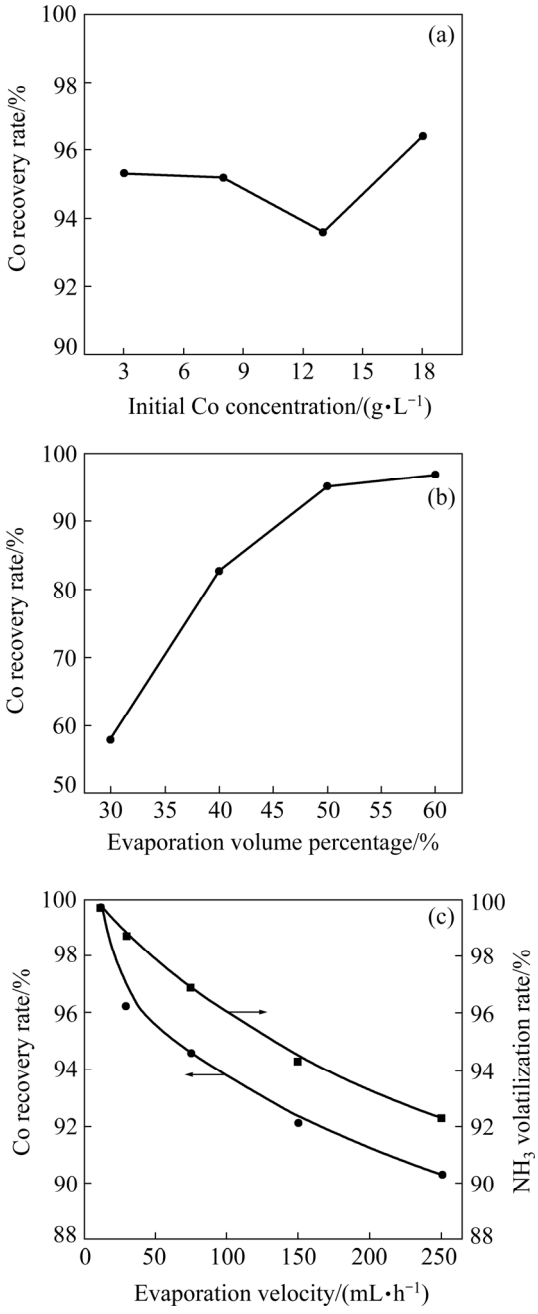

Fig. 2 Effect of initial Co concentration (a), evaporation volume percentage (b), and evaporation velocity (c) on Co recovery rate

concentration in the AAC solution on the Co recovery rate under constant conditions of 50% evaporation volume percentage and 75 mL/h evaporation velocity. At different initial Co concentrations, the Co recovery rate is over 93%, that is, the NH_3 distillation process has a wide range of applicability to the initial Co concentration in the AAC solution. Figure 2(b) shows the effect of evaporation volume percentage on Co recovery under the conditions of 17 g/L initial Co concentration and 75 mL/h evaporation velocity. When the evaporation volume percentage is 50% of the initial solution volume, the Co recovery rate reaches 94.6%. Although the Co recovery rate still increases with the increase of evaporation volume, given that the residual liquor needs to be returned for leaching, 50% of the evaporation volume percentage is appropriate.

Figure 2(c) shows the effect of the evaporation velocity on Co recovery rate and NH_3 volatilization rate under the conditions of 50% evaporation volume percentage and 17 g/L initial Co concentration. The results show that the Co recovery and NH_3 volatilization rate decrease to a certain extent after evaporation velocity increases. Because of the increase in the evaporation rate of H_2O, a part of NH_3 is not evaporated, and the volume of the solution decreases rapidly. Although a low evaporation velocity leads to a high Co recovery rate, NH_3 distillation time greatly increases when the evaporation velocity is lower than 75 mL/h. Evaporation velocity also influences the morphology of the precursor. When evaporation velocities are 15 and 30 mL/h, the precursors show irregular and aggregated morphologies, as shown in Figs. 3(a) and (b), respectively. When evaporation velocity reaches at least 75 mL/h, the precursors grow into microspheres with particle sizes of 1−2 μm (Figs. 3(c) and (d)). Therefore, an evaporation velocity of 75 mL/h is appropriate for NH_3 distillation, and 96.3% NH_3 and 94.6% Co can be recovered under the conditions.

3.3 Precursor composition

In NH_3 distillation, many particles aggregate into amorphous precipitates because the formation rate of crystal nuclei is higher than the directional growth rate of the precursor [24]. Figure 4 shows the SEM image and EDS mapping of the precursor. The precursor is mainly composed of Co, O, C, and N, which are evenly distributed in the precursor. Figure 5(a) displays the FT-IR spectrum of the precursor. The broad peaks at 3110.17 and 1453.42 cm^{-1} are attributed to the stretching vibration peaks of N—H [25]. This result indicates that ammonium still exists in the precursor. The

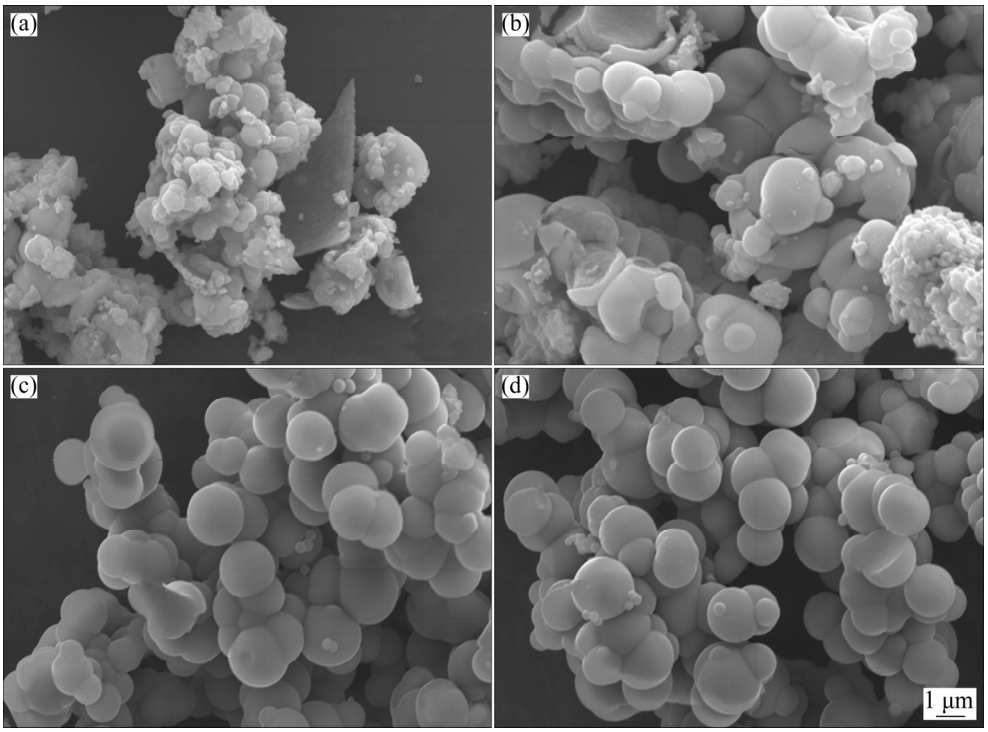

Fig. 3 Effect of evaporation velocity on morphology of precursor: (a) 15 mL/h; (b) 30 mL/h; (c) 75 mL/h; (d) 150 mL/h

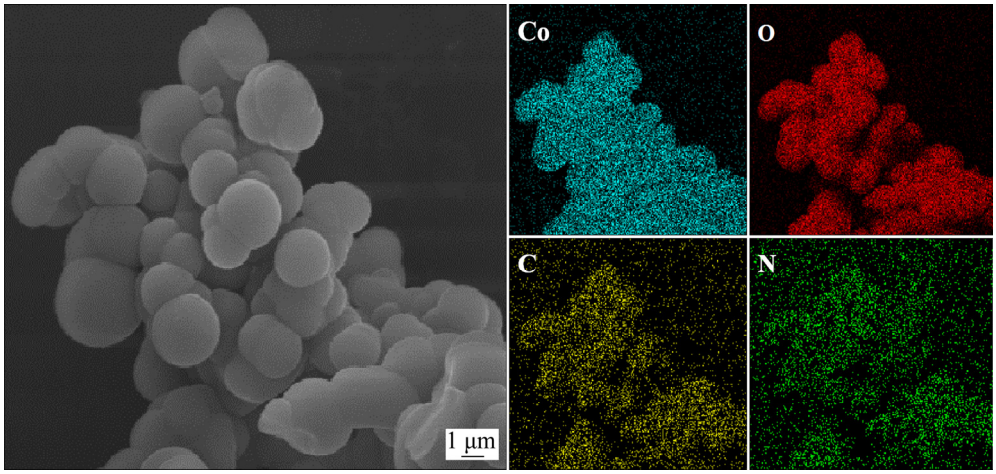

Fig. 4 SEM image and EDS mapping of precursor

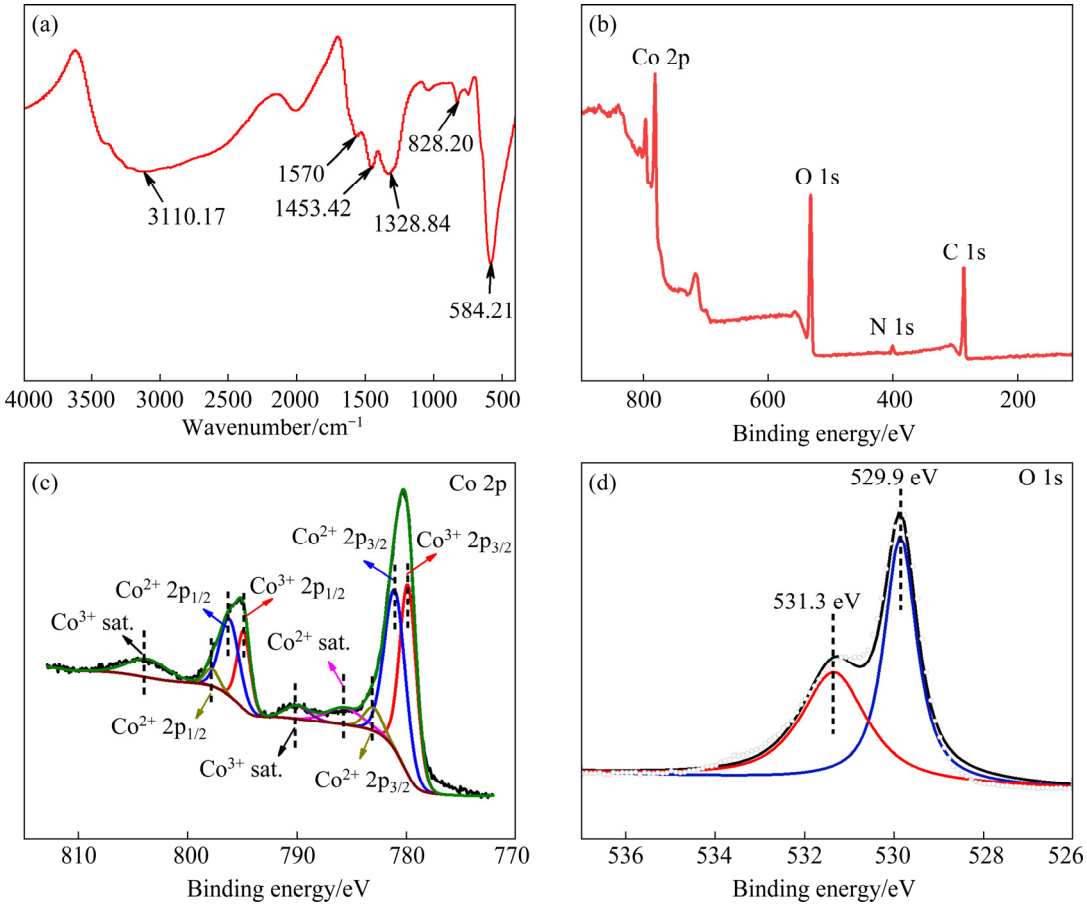

Fig. 5 FT-IR (a) and XPS (b−d) spectra of precursor: (b) Full spectrum; (c) Co 2p; (d) O 1s

peaks at 1570 and 1328.84 cm^{-1} are CO_3^{2-} stretching vibrations, the peak at 828.20 cm^{-1} is CO_3^{2-} bending vibration [26,27], and the peak at 584.21 cm^{-1} is the Co−CO_3^{2-} lattice vibration absorption.

Figure 5(b) shows the XPS full spectrum of the precursor, the peaks of Co 2p, O 1s, N 1s, and C 1s can be seen, which are consistent with the results of the EDS mapping. Figure 5(c) displays the peaks of Co 2p. 779.8, 794.8, 790, and 803 eV are the characteristic peaks of Co(III), and 781.1, 796.2, 783.1, 797.7, and 785.7 eV are the characteristic peaks of Co(II) [28]. Given that Co exists in the initial solution in the form of $Co(NH_3)_6^{3+}$, O_2 is found by detecting the generated gas according to Fig. 6. Reaction (2) may occur during the NH_3 distillation process. Furthermore,

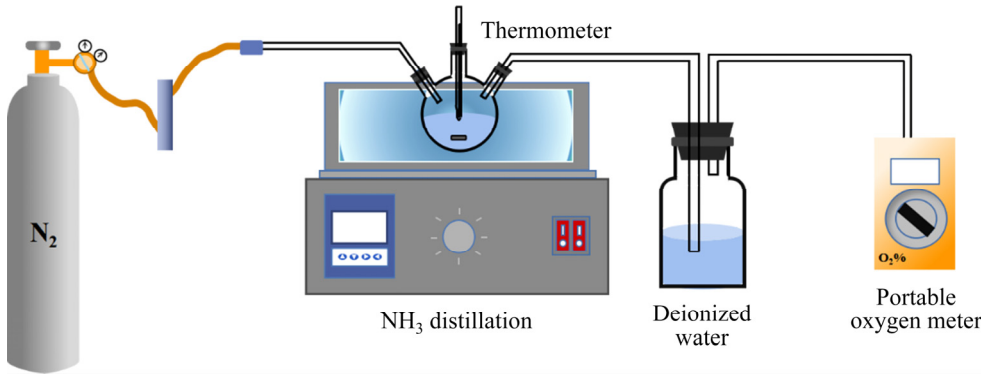

Fig. 6 Device of O_2 detection

the Gibbs free energy change (ΔG) of Reaction (2) (ΔG=1353.097−3.98T) is less than 0 when the temperature is higher than 67 °C, and the actual solution temperature is higher than 94 °C in the experiment. Therefore, Co(II) is present in the precursor because of the process described in Reaction (2). The O 1s spectra are shown in Fig. 5(d). The peak at 529.9 eV corresponds to oxygen in water adsorbed on the precursor surface, which can be attributed to the adsorption of H_2O in the air by the sample during the test [29]. The peak at 531.3 eV corresponds to the oxygen in CO_3^{2-} [30]. By combining the reaction system and above analysis, it can be inferred that the precursor is cobalt carbonate ammonium compound salt $((NH_4)_x Co_y^{(III)} Co_{(1-y)}^{(II)} (CO_3)_z)$.

$$4Co(NH_3)_{6(aq)}^{3+} + 4OH_{(aq)}^{-} \rightarrow 4Co_{(aq)}^{2+} + 24NH_{3(g)} + O_{2(g)} + 2H_2O_{(l)} \quad (2)$$

3.4 Formation mechanism of precursor

In the NH_3 distillation process, changes of Co concentration and NH_3 volatilization rate in the solution at different time were recorded under optimal conditions. Evaporated cobalt ammonia complex is different from the crystallization of generally saturated compounds. Firstly, the balance between Co and NH_3 is broken, NH_3 overflows, and the stability of the cobalt−ammonia complex changes with increasing solution temperature. Then, a large number of ions in the supersaturated solution form crystal nuclei and gradually grow into particles. As shown in Fig. 7, a large amount of NH_3 overflows and Co concentration slightly changes within 0−27 min. At this stage, the number of crystal nuclei that form in the solution is limited, and the formation speed of the precursor is slow.

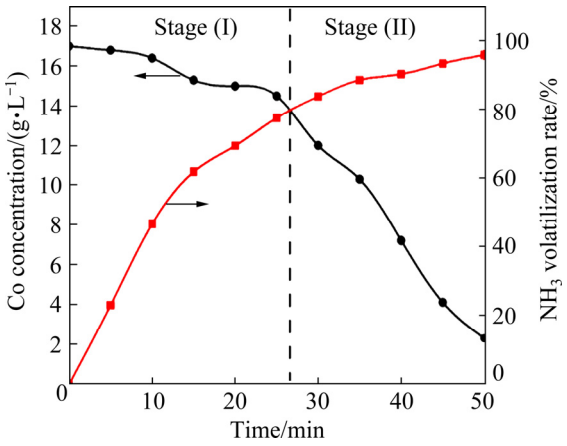

Fig. 7 Changes of Co concentration and NH_3 volatilization rate during entire NH_3 distillation process

After 27 min, the solution is supersaturated, a large number of ions accumulate on the surface of the crystal nucleus and finally form a black precursor, and Co concentration decreases rapidly during this process.

Therefore, the precursor precipitation process consists of two stages: the first stage is the breaking of the chemical bond between cobalt−ammonia complexes and volatilization of NH_3 and H_2O, as shown in Reactions (3) and (4). Moreover, part of the $Co(NH_3)_6^{3+}$ is reduced to Co^{2+} according to Reaction (2). Through Reactions (2)−(4), the solution is gradually supersaturated, and some ions collide, are adsorbed, and fuse to form crystal nucleus during stirring. In the second stage, a large number of NH_4^+, Co^{2+}, Co^{3+}, and CO_3^{2-} gather on the surface of the crystal nucleus, and a dynamic exchange and substitution process between a part of the ions and defects on the surface of the crystal nucleus and gradually precipitate out of the solution. The reaction can be described in Reaction (5). Figure 8 shows the SEM images of the precipitates

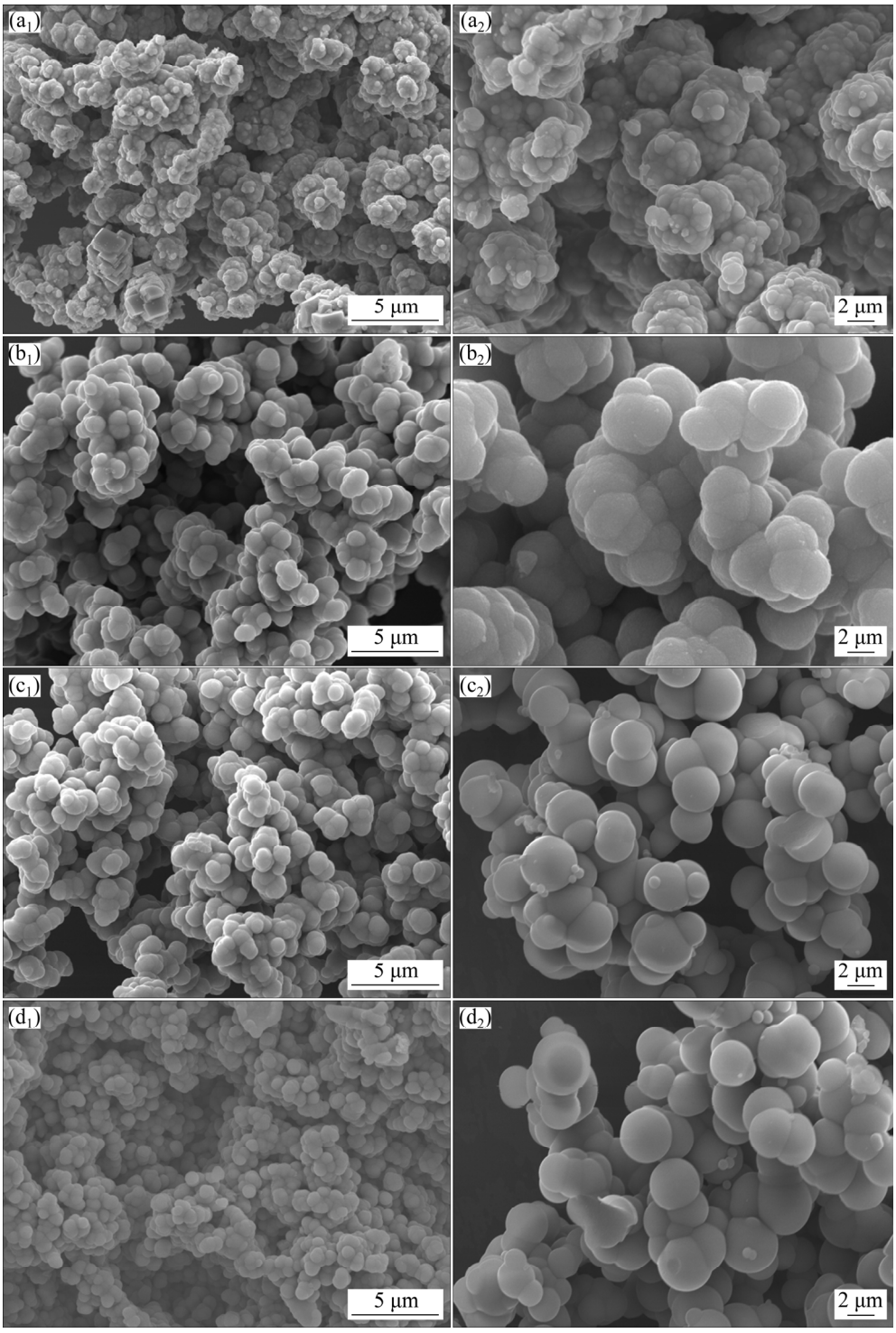

Fig. 8 Morphologies of precipitates at different time: (a_1, a_2) 20 min; (b_1, b_2) 30 min; (c_1, c_2) 40 min; (d_1, d_2) 50 min

obtained at different NH_3 distillation time under the fixed conditions of evaporation temperature and initial cobalt concentration. In the initial stage, the nucleation rate is faster than the crystal growth rate, and the precipitates have not fully grown, presenting large clump shapes (Figs. 8(a_1, a_2)). However, the clear microsphere-like outline is observed at 30 min, but there are still obvious agglomerations (Figs. 8(b_1, b_2)). At 40 min, the microspheres gradually become fuller, and the morphology does not change significantly at 40−50 min, which means the growth process has been completed basically at 40 min, as shown in Figs. 8(c_1, c_2) and (d_1, d_2). Therefore, the changes of the precipitate morphologies are not obvious at 40 and 50 min. Figure 9 displays the schematic

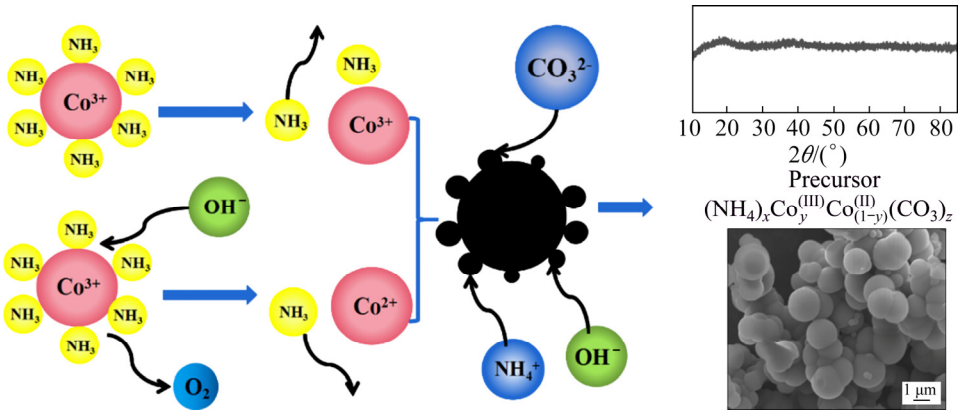

Fig. 9 Schematic representation of precursor precipitation

representation of precursor precipitation.

$$Co(NH_3)_{6(aq)}^{3+} \rightarrow Co_{(aq)}^{3+} + 6NH_{3(l)} \quad (3)$$

$$NH_{3(l)} \rightarrow NH_{3(g)} \quad (4)$$

$$yCo_{(aq)}^{3+} + (1-y)Co_{(aq)}^{2+} + zCO_{3(aq)}^{2-} + xNH_{4(aq)}^{+} \rightarrow (NH_4)_x Co_y^{(III)} Co_{(1-y)}^{(II)} (CO_3)_{z(s)} \quad (5)$$

3.5 Transformation of Co_3O_4 from precursor

The thermochemical characteristics of the precursor are examined through TG−DSC. The DSC curve in Fig. 10 shows no evident endothermic or exothermic peak at 0−100 °C. The first endothermic peak appears at 199.63 °C. At 316 °C, the precursor completely loses mass because of precursor decomposition for Co_3O_4 production, and the mass loss rate is 25.32%. When the temperature reaches 671.69 °C, the second endothermic peak appears, but no change in mass occurs, indicating that only a physical state transition occurs.

The effect of roasting temperature on roasting products was studied according to the TG−DSC results. The precursor was roasted in a muffle furnace at 300, 500, and 750 °C for 3 h, and the XRD patterns of the roasted products are shown in Fig. 11(a). The diffraction peaks of the Co_3O_4 appear at 300 °C. When the roasting temperature is 500 and 750 °C, respectively, the intensity of diffraction peaks of Co_3O_4 slightly increases. Figure 11(b) displays the enlarged view of the roasted products at 300 and 750 °C (2θ=30°−40°). The diffraction peaks of Co_3O_4 at 750 °C shift. Although the roasted products at both temperatures are Co_3O_4, $CoCo_2O_4$ corresponding to the PDF

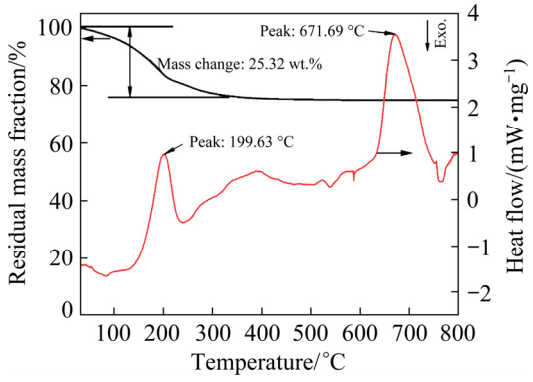

Fig. 10 TG−DSC curves of precursor

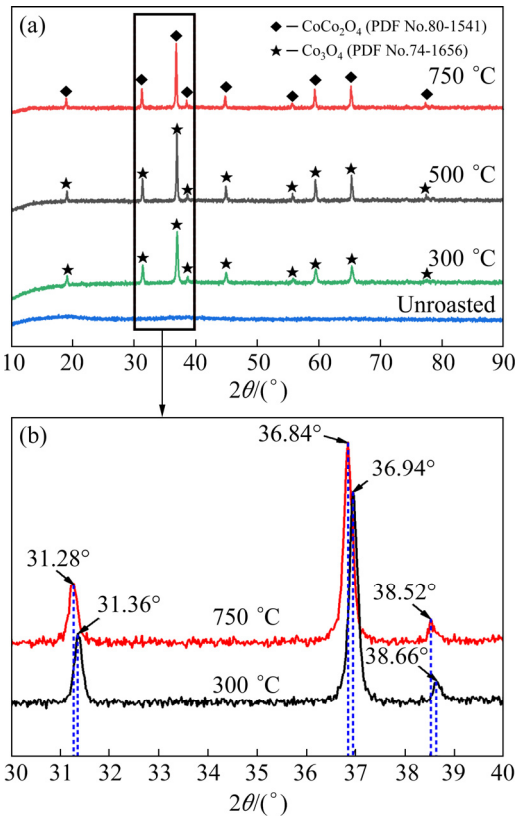

Fig. 11 XRD patterns of precursor roasted at different temperatures

No. 80-1541 card is a high-spin spinel structure Co_3O_4, which belongs to the high-temperature phase [31,32]. Meanwhile, the common spinel structure Co_3O_4 (PDF No. 74-1656) is in a low-spin state. The temperature at which Co_3O_4 changes from a low-spin ground state to a high-spin state is 627 °C according to previous research [33]. Therefore, the existence of a broad endothermic peak in the DSC curve between 600 and 750 °C may be related to the physical transition of the spin state.

Figure 12 shows the SEM images of Co_3O_4 at different roasting temperatures. Compared with the morphology of the precursor (Fig. 12(a)), the morphologies of roasted products at 300 °C (Fig. 12(b)) and 500 °C (Fig. 12(c)) show no substantial change, and Co_3O_4 remains micro-spherical, with a particle size of 1−2 μm. The reason is that the thermal decomposition reaction usually occurs at crystal defects, such as dislocations, impurities, and crystal surfaces. Moreover, the newly formed crystal nucleus has an inheritance to the precursors [34], and thus the morphology of Co_3O_4 remains similar to that of the precursors. In phase transformation, NH_4^+ and CO_3^{2-} disintegrate from the lattice of the reactants and rapidly release CO_2 and NH_3. The release of these gases causes micropores and cracks on the surface of the precursor. When the roasting temperature is 750 °C, particle agglomeration is obvious (Fig. 12(d)), the average particle size significantly increases, and the specific surface area decreases sharply from 100.485 to 4.523 m^2/g. Moreover, as shown in Table 3, the pore diameter increases with the roasting temperature increasing from 300 to 750 °C. However, the surface area and pore volume of Co_3O_4 decrease with the increase of roasting temperature owing to the particle agglomeration and pore structure collapse [35].

Figure 13(b) displays the pore size distribution

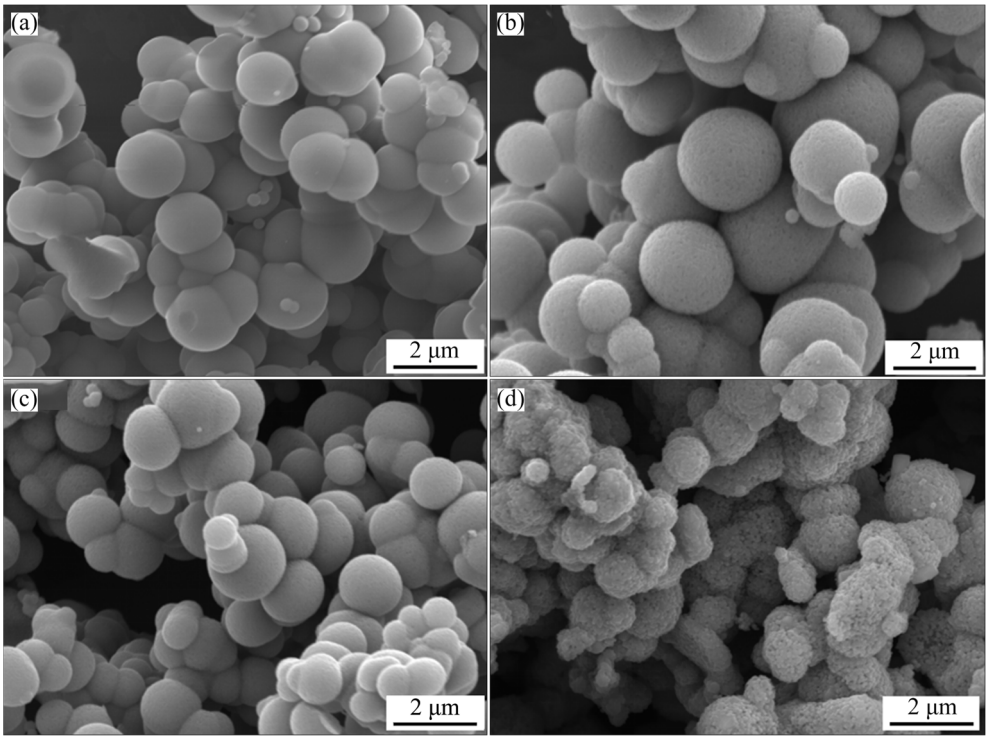

Fig. 12 SEM images of Co_3O_4 roasted at different temperatures: (a) Unroasted; (b) 300 °C; (c) 500 °C; (d) 750 °C

Table 3 Average particle sizes, BET surface areas, pore diameters, and pore volumes of roasted products at different temperatures

Temperature/°C	Average particle size/nm	Surface area/($m^2 \cdot g^{-1}$)	Pore diameter/nm	Pore volume/($cm^3 \cdot g^{-1}$)
300	59.710	100.485	3.062	0.0769
500	387.976	15.465	14.115	0.0542
750	1326.550	4.523	28.300	0.032

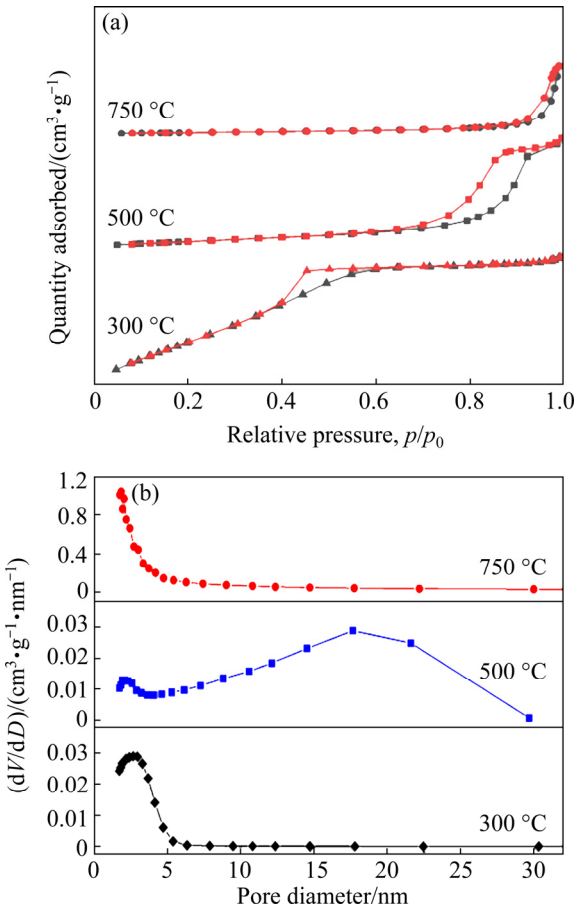

Fig. 13 N_2 adsorption−desorption isotherms (a) and pore size distribution (b) of roasted products at different temperatures

of Co_3O_4 at different roasting temperatures. Co_3O_4 presents a porous structure, and the pore diameter is less than 5 nm at 300 °C. When the roasting temperature increases, the pore diameter also increases significantly, and it can reach 28.3 nm at the roasting temperature of 750 °C. Figure 13(a) shows the N_2 adsorption–desorption isotherms of Co_3O_4 at different roasting temperatures. The isotherm of 300 °C is classified as Type I according to the IUPAC classification and is a typical adsorption feature of a microporous solid. The isotherms of 500 and 750 °C are classified as Type IV and are the typical adsorption features of a mesoporous structure [35,36]. The results are consistent with those of pore diameters in Table 3 and morphology changes in Co_3O_4 in Fig. 12. According to the above analysis, Co_3O_4 with different physical states and properties can be obtained at different temperatures.

In this work, a process of using NH_3 distillation and phase transformation for recovering Co and obtaining microspherical Co_3O_4 from AAC solutions was proposed. NH_3 and the residual liquid were recycled, and the microspherical Co_3O_4 was obtained at a low temperature. The microspherical Co_3O_4 can be used in $LiCoO_2$ production or as an energy storage electrode. Compared with the traditional process of adding Na_2S or $(NH_4)_2S$ to generate CoS or adding reducing agent and NaOH to generate $Co(OH)_2$, the proposed method does not need the addition of chemical reagents and no wastewater is produced, and is thus suitable for industrial production.

4 Conclusions

(1) Thermodynamic analysis shows that the increase in c_N and the decrease in c_C are conducive to the dissolution of Co. The theoretical solubility of Co is maximized when pH is increased to 10. Co was efficiently recovered from the AAC solution through NH_3 distillation. 94.6% Co and 96.3% NH_3 were recovered under optimal conditions of evaporation velocity of 75 mL/h and evaporation volume percentage of 50%.

(2) Mechanism analysis shows that the process can be divided into two stages: (1) $Co(NH_3)_6^{3+}$ decomposes and releases NH_3, and a fraction of $Co(NH_3)_6^{3+}$ is reduced to Co^{2+}. Some ions collide with each other, are adsorbed, and fuse to form crystal nuclei during stirring; (2) a large number of ions accumulate on the surface of the formed crystal nuclei and gradually grow into microspherical particles. Finally, cobalt carbonate ammonium compound salt $((NH_4)_xCo_y^{(III)}Co_{(1-y)}^{(II)}(CO_3)_z)$ precursor forms.

(3) The precursor was roasted at 300 °C for 3 h. Microspherical Co_3O_4 with a BET surface area of 100.485 m^2/g, pore diameter of 3.062 nm, and average particle size of 59.710 nm was successfully prepared. At a roasting temperature of 750 °C, Co_3O_4 with a mesoporous structure and high-spin state was obtained.

Acknowledgments

This work was financially supported by the National Natural Science Foundation of China (Nos. 52034002, U1802253, 51974025), and the Fundamental Research Funds for the Central Universities, China (No. FRF-MP-20-04).

References

[1] WANG Shuo-bing, WANG Chao, LAI Feng-jiao, YAN Feng, ZHANG Zuo-tai. Reduction-ammoniacal leaching to recycle lithium, cobalt, and nickel from spent lithium-ion batteries with a hydrothermal method: Effect of reductants and ammonium salts [J]. Waste Management, 2020, 102: 122−130.

[2] SETHURAJAN M, GAYDARDZHIEV S. Bioprocessing of spent lithium-ion batteries for critical metals recovery—A review [J]. Resources, Conservation and Recycling, 2021, 165: 105225−105238.

[3] BABBITT C W. Sustainability perspectives on lithium-ion batteries [J]. Clean Technologies and Environmental Policy, 2020, 22(6): 1213−1214.

[4] ZHU Shu-guang, HE Wen-zhi, LI Guang-ming, ZHOU Xu, ZHANG Xiao-jun, HUANG Ju-wen. Recovery of Co and Li from spent lithium-ion batteries by combination method of acid leaching and chemical precipitation [J]. Transactions of Nonferrous Metals Society of China, 2012, 22(9): 2274−2281.

[5] LV Wei-guang, WANG Zhong-hang, CAO Hong-bin, SUN Yong, ZHANG Yi, SUN Zhi. A critical review and analysis on the recycling of spent lithium-ion batteries [J]. ACS Sustainable Chemistry & Engineering, 2018, 6(2): 1504−1521 .

[6] MA Ya-yun, TANG Jing-jing, WANALDI R, ZHOU Xiang-yang, WANG Hui, ZHOU Chang-you, YANG Juan. A promising selective recovery process of valuable metals from spent lithium-ion batteries via reduction roasting and ammonia leaching [J]. Journal of Hazardous Materials, 2020, 402(15): 123491−123501.

[7] HU Jun-tao, ZHANG Jia-liang, LI Hong-xu, CHEN Yong-qiang, WANG Cheng-yan. A promising approach for the recovery of high value-added metals from spent lithium-ion batteries [J]. Journal of Power Sources, 2017, 351: 192−199.

[8] YANG Cheng, ZHANG Jia-liang, YU Bo-yuan, HUANG Hao, CHEN Yong-qiang, WANG Cheng-yan. Recovery of valuable metals from spent $LiNi_xCo_yMn_zO_2$ cathode material via phase transformation and stepwise leaching [J]. Separation and Purification Technology, 2021, 267: 118609−118618.

[9] CHEN Xiang-ping, ZHOU Tao, KONG Jiang-rong, FANG Hua-xiong, CHEN Yong-bin. Separation and recovery of metal values from leach liquor of waste lithium nickel cobalt manganese oxide based cathodes [J]. Separation and Purification Technology, 2015, 141(12): 76−83.

[10] HIGUCHI A, ANKEI N, NISHIHAMA S, YOSHIZUKA K. Selective recovery of lithium from cathode materials of spent lithium ion battery [J]. JOM, 2016, 68(10): 2624−2631.

[11] YANG Cheng, ZHANG Jia-liang, CAO Zhi-he, JING Qian-kun, WANG Cheng-yan. Sustainable and facile process for lithium recovery from spent $LiNi_xCo_yMn_zO_2$ cathode materials via selective sulfation with ammonium sulfate [J]. ACS Sustainable Chemistry & Engineering, 2020, 8(41): 15732−15739.

[12] PARHI P K, PANIGRAHI S, SARANGI K, NATHSARMA K C. Separation of cobalt and nickel from ammoniacal sulphate solution using Cyanex 272 [J]. Separation and Purification Technology, 2008, 59(3): 310−317.

[13] WANG Cheng-yan. Separation of Cu, Ni, and Co from ammonia solution by solution extraction [J]. Nonferrous Metals, 2002, 54(1): 23−26. (in Chinese)

[14] CHEN Sheng-li, GUO Xue-yi, SHI Wen-tang, LI Dong. Extraction of valuable metals from low-grade nickeliferous laterite ore by reduction roasting−ammonia leaching method [J]. Journal of Central South University of Technology, 2010, 17(4): 765−769.

[15] HURST F J. Separation of cobalt from nickel in ammonia-ammonium carbonate solutions using pressurized ion exchange [J]. Hydrometallurgy, 1976, 1(4): 319−338.

[16] QIAN Dong, WANG Kai-yi, PAN Chun-yue, TANG You-gen, CAI Chun-lin, PAN Jin-zhi. Separation of nickel, cobalt and copper by solvent extraction with P204 [J]. Transactions of Nonferrous Metals Society of China, 2001, 11(5): 803−805.

[17] LI Ben-sheng, WU Cai-bin, HU Die, XU Jin-dong, ZHANG Tao, TONG Jia-qi, FANG Xin. Copper extraction from the ammonia leach liquor of spent lithium-ion batteries for regenerating $LiNi_{0.5}Co_{0.5}O_2$ by co-precipitation [J]. Hydrometallurgy, 2020, 193: 105310−105316.

[18] MIAO Ze-lin, ZHAN Jing, XU Zi-wei. Thermodynamic simulation of metal behaviors in Cu^{2+}–Ni^{2+}–NH_3–NH_4^+–$C_2O_4^{2-}$–H_2O system [J]. Transactions of Nonferrous Metals Society of China, 2021, 31(5): 1475−1483.

[19] MA Li-wen, NIE Zuo-ren, XI Xiao-li, LI Xiao-kang. Theoretical simulation and experimental study on nickel, cobalt, manganese separation in complexation–precipitation system [J]. Separation & Purification Technology, 2013, 108: 124−132.

[20] PRANOWO H D, WIJAYA K, SETIAJI B, JANU R S. Determination of many-body effect of $[Co(NH_3)_n]^{2+}$ (n=1−6) complexes base on abinitio calculations [J]. Indonesian Journal of Chemistry, 2010, 2(1): 1−7.

[21] OSSEO-ASARE K, LEE J W, KIM H S, PICKERING H W. Cobalt extraction in ammoniacal solution: Electrochemical effect of metallic iron [J]. Metallurgical Transactions B, 1983, 14(4): 571−576.

[22] KU H, JUNG Y, JO M, PARK S, KIM S, YANG D, RHEE K, AN E M, SOHN J, KWON K. Recycling of spent lithium-ion battery cathode materials by ammoniacal leaching [J]. Journal of Hazardous Materials, 2016, 313: 138−146.

[23] ASSELIN E. Thermochemistry of the Fe−Ni−Co−NH_3−H_2O system: A review [J]. Minerals & Metallurgical Processing, 2011, 28: 169−175.

[24] POTAPOV V V. Precipitation of amorphous silica from a high-temperature hydrothermal solution [J]. Glass Physics & Chemistry, 2004, 30(1): 73−81.

[25] ARANA J, RENDON E T, RODRIGUEZ J M D, MELIAN J A H, DIAN O G, PENA J P. FTIR study of the photocatalytic degradation of NH_4^+ determination wastes [J]. Journal of Photochemistry and Photobiology A: Chemistry, 2002, 148(1/2/3): 215−222.

[26] FROST R L, LÓPEZ A, WANG L N, SCHOLZ R, SAMPAIO N P. SEM, EDX and Raman and infrared spectroscopic study of brianyoungite $Zn_3(CO_3,SO_4)(OH)_4$ from Esperanza Mine, Laurion District, Greece [J]. Spectrochimica Acta (Part A): Molecular and Biomolecular Spectroscopy, 2015, 149: 279−284.

[27] PASUPULETY N, AL-ZAHRANI A A, DAOUS M A, PODILA S, DRISS, H. A study on highly active Cu−Zn−Al−K catalyst for CO_2 hydrogenation to methanol [J]. Arabian Journal of Chemistry, 2020, 14(2): 102951−102960.

[28] WANG Bing, WANG Jun-hua, SHANG Dun-sheng, CHANG Ai-ming, YAO Jin-cheng. Sintering temperature and XPS analysis of $Co_{2.77}Mn_{1.71}Fe_{1.10}Zn_{0.42}O_8$ NTC ceramics [J]. Materials Chemistry and Physics, 2020, 239: 122098−122104.

[29] LIN Su-fen, ZHANG Ning, WANG Fu-chen, LEI Ju-ying, ZHOU Liang, LIU Yong-di, ZHANG Jin-long. Carbon vacancy mediated incorporation of Ti_3C_2 quantum dots in a 3D inverse opal g-C_3N_4 schottky junction catalyst for photocatalytic H_2O_2 production [J]. ACS Sustainable Chemistry & Engineering, 2021, 9(1): 481−488.

[30] CHEN Shan-hu, GAO Yi, LAN Li, ZHAO Ming, SHOU Zhong-hua. Preparation of mesoporous CeO_2 with high thermal stability by ammonium carbonate hydrolysis method [J]. Chinese Journal of Inorganic Chemistry, 2013, 29(10): 2231−2238. (in Chinese)

[31] CHEN M, HALLSTEDT B, GAUCKLER L J. Thermodynamic assessment of the Co−O system [J]. Journal of Phase Equilibria, 2003, 24(3): 212−227.

[32] LIU X, PREWITT C T. High-temperature X-ray diffraction study of Co_3O_4: Transition from normal to disordered spinel [J]. Physics and Chemistry of Minerals, 1990, 17(2): 168−172.

[33] SONG Li-ming, ZHANG Shu-juan, CHEN Bin, ZHANG Shu-na, SUN Dong-lan. A facile hydrothermal route to spinel $CoCo_2O_4$ nanotubes and porous nanostructures without assisted surfactants and templates [J]. Materials Letters, 2009, 63(16): 1377−1380.

[34] ZHANG Li, WANG Zheng-bo, YU Xian-wang, WU Chong-xu, SHAN Cheng. Thermal dissociation mechanism and morphological inheritance of basic cobalt carbonate [J]. Materials Science Engineering of Powder Metallurgy, 2010, 15(6): 679−684. (in Chinese)

[35] SHAO Shuang, MA Bao-zhong, ZENG Lei, XING Ping, LIU Bao, WANG Cheng-yan. Copper selective separation and nanoporous copper oxide preparation from waste copper-clad aluminum scraps [J]. Hydrometallurgy, 2020, 192: 105287−105293.

[36] XING Ping, WANG Cheng-yan, ZENG Lei, MA Bao-zhong, WANG Ling, CHENG Yong-qiang, YANG Cheng. Lithium extraction and hydroxysodalite zeolite synthesis by hydrothermal conversion of α-spodumene [J]. ACS Sustainable Chemistry & Engineering, 2019, 7(10): 9498−9505.

从废旧锂离子电池氨浸液中回收钴并制备微球状四氧化三钴

郁建成[1,2]，马保中[1,2]，邵 爽[1,2]，王成彦[1,2]，陈永强[1,2]，张文娟[1,2]

1. 北京科技大学 钢铁冶金新技术国家重点实验室，北京 100083；
2. 北京科技大学 冶金与生态工程学院，北京 100083

摘 要：提出一种通过蒸氨和相变从氨性溶液中回收钴并制备微球状 Co_3O_4 的工艺。作为热力学基础，首先分析钴在不同 NH_3 和 CO_3^{2-} 浓度中的溶解度；然后讨论不同的蒸氨条件对钴回收率的影响。通过蒸氨，可以回收超过94%的钴和96%的氨，钴以碳酸钴铵复盐形式沉淀。前驱体沉淀机理的分析结果表明，钴的析出过程有两个阶段，并且在第二阶段的沉淀速度明显加快。在相变过程中，研究温度对焙烧产物的影响，在 300 ℃时可获得具有微孔结构的微球状 Co_3O_4；而在 750 ℃时可获得具有介孔结构和高自旋状态的 Co_3O_4。

关键词：废旧锂离子电池；蒸氨；钴回收；机理分析；Co_3O_4 制备

(Edited by Wei-ping CHEN)